Second-Order Sliding-Mode Controlled Synchronous Buck DC–DC Converter

Rui Ling, *Member, IEEE*, Dragan Maksimovic, *Fellow, IEEE*, and Ramon Leyva, *Member, IEEE*

***Abstract*—In this paper, second-order sliding-mode (SOSM) control approach is applied to synchronous buck dc–dc converters. The proposed SOSM controller can stabilize synchronous buck dc–dc converters using a simple digital state-machine structure, without requiring current sensing or an integral term in the control loop. The SOSM controller results in fast step-load and start-up transient responses, and is robust against parameter uncertainties. Fast transients and current limitation during start up can be accomplished by adjusting one controller parameter. Furthermore, a hysteresis method is introduced to control the switching frequency. The proposed approach is verified by experimental results on a 1.25-V 10-A prototype.**

***Index Terms*—DC–DC converter, digital control, second-order sliding-mode (SOSM) control, state-machine, voltage feedback.**

I. Introduction

DC–DC converters are commonly controlled using pulse width modulation, where switch control signals are determined based on sensing the output voltage and other state variables, and by employing compensators designed using converter small-signal averaged models and frequency-domain techniques [1], [2]. The compensator usually uses an output error integral term in order to ensure zero steady-state error. An advantage of this approach is that the pulse width modulator and the converter operate at a constant switching frequency. Since the design is based on small-signal techniques [2], the prescribed dynamic performances are only ensured around a certain equilibrium point. Furthermore, the presence of an integral term in some cases implies a slow response against disturbances.

Various large-signal-based approaches have been considered to improve transient responses and robustness of closed-loop controlled dc–dc converters, including hybrid digital adaptive control [3], proximate time-optimal control [4], boundary control [5], [6], or raster surface control [7]. In particular, sliding-mode control (SMC) has attracted significant attention in dc–dc control applications. SMC may be used to characterize the system under both small- and large- signal conditions [8], and provide robust responses of the output against uncertainties and disturbances [9], [10]. Traditional SMC and various extensions have been successfully applied to dc–dc converters [8], [11]–[15]. Traditional SMC uses a certain switching surface $s = 0$, which divides the state space into two subspaces, and control from the set $\{U^+, U^-\}$ in each subspace, respectively, to constrain the dynamics ideally at $s = 0$. This approach requires that the surface s be of relative degree 1, and also requires a stable behavior of the ideal sliding dynamics [9], [10]. Note that relative degree indicates the number of times by which the output is differentiated until the input appears explicitly [16]. In the context of single-input single-output linear time-invariant systems, the relative degree is the difference between the order of the denominator and the order of numerator of the control to output transfer function. Applied to a dc–dc converter, the traditional SMC in most cases requires that the switching surface $s = 0$ be a combination of the output voltage and an inductor or capacitor current. In general, current sensing leads to increased noise sensitivity and increased cost. Techniques, such as boundary control [5], [6] employ a higher order switching surface to achieve fast dynamic responses, but switching surface evaluation still requires current sensing.

High-order sliding-mode (HOSM) is an extension of traditional SMC. For a smooth function s (it is consider as the sliding variable), the motion on the set $s = \dot{s} = \cdots = s^{(r-1)} = 0$ is called *r*th-order sliding mode [26], [27] if the successive total time derivatives $s, \dot{s}, \ldots, s^{(r-1)}$ are continuous functions, and $s = \dot{s} = \cdots = s^{(r-1)} = 0$ is a nonempty set that consists locally of Filippov trajectories [28]. Traditional first-order sliding mode is of the first order [27], where s is continuous and $\dot{s}$ is discontinuous. Second-order sliding-mode (SOSM) belongs to a class of HOSM, where s and $\dot{s}$ are continuous and $\ddot{s}$ is discontinuous. The surface in first-order SMC is a line $s = 0$ in phase plane $s - \dot{s}$, while in SOSM control it is a point, i.e., the origin $s = \dot{s} = 0$ in the phase plane $s - \dot{s}$. This feature impacts the asymptotic performance. During a transient, a system trajectory under traditional first-order SMC reaches the surface first, and then, moves along the surface to approach the origin in the $s - \dot{s}$ phase plane. Note that the first-order SMC needs the information of $\dot{s}$ and s to stabilize systems of relative degree 2 [20], such as the buck dc–dc converter. In contrast, under SOSM control, a trajectory in the phase plane $s - \dot{s}$ can reach the surface (i.e., the origin) directly. Some SOSM control algorithms require only s for stabilizing systems with relative degree 2.

Manuscript received November 24, 2014; revised March 22, 2015; accepted April 22, 2015. Date of publication May 8, 2015; date of current version November 16, 2015. This work was supported in part by the National Natural Science Foundation of China (61203097), China Postdoctoral Science Foundation (2013T60840 and 2012M511907), Fundamental Research Funds for the Central Universities in China (106112013CDJZR170003), AQSIQ Science and Technology Projects (2012IK029), and Chongqing Application Development Plan Project in China CSTC2014YYKFA80017. Recommended for publication by Associate Editor S. K. Mazumder.

R. Ling is with the Key Laboratory of Dependable Service Computing in Cyber Physical Society (Chongqing University), Ministry of Education, and the College of Automation, Chongqing University, Chongqing 400030, China (e-mail: rui.ling@cqu.edu.cn).

D. Maksimovic is with the Department of Electrical, Computer and Energy Engineering, University of Colorado Boulder, Boulder, CO 80309 USA (e-mail: maksimov@colorado.edu).

R. Leyva is with the Departament d'Enginyeria Electrònica, Elèctrica i Automàtica, Universitat Rovira i Virgili, 43007 Tarragona, Spain (e-mail: ramon.leyva@urv.cat).

Color versions of one or more of the figures in this paper are available online at http://ieeexplore.ieee.org.

Digital Object Identifier 10.1109/TPEL.2015.2431193

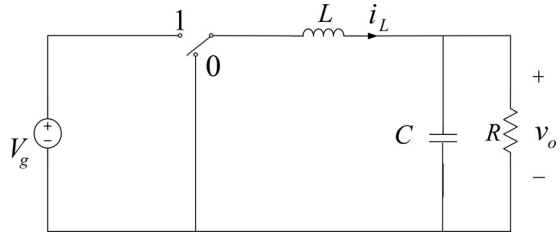

Fig. 1. Synchronous buck converter.

The proposed controller is implemented by means of a state machine consisting of four states based on second-order SMC theory using only the knowledge of s [23]. The output voltage is the only required feedback signal. The approach can result in robust behavior with respect to parameter uncertainties and load disturbances in the converter. Current sensing or an integral term in the control loop are not required.

The SOSM approach described in this paper is based on theoretical contributions, which are briefly summarized here. Application of a suboptimal SOSM algorithm to control a buck converter has been reported proposed in [17]. In this case, however, the controller is designed by means of an averaged model. In addition, the capacitor current is used as a component of the switching surface. A boost converter for a PEM fuel cell is controlled using a supertwist algorithm in [18]. Similarly, a three-phase full-bridge boost converter is controlled using current observers based on supertwist algorithms in [19]. Only simulation results have been reported in these earlier works. This paper shows how an improved suboptimal algorithm [20] can be applied practically to a synchronous buck dc–dc converters. Furthermore, a new hysteresis method is proposed to control the switching frequency.

This paper is organized as follows. SOSM control for synchronous buck dc–dc converters is introduced in Section II. The architecture of SOSM controller and basic principles are presented in Section III. The controller design for synchronous buck converters is presented in Section IV. Experimental verification for a 1.25-V 10-A synchronous buck converter is given in Section V. Section VI concludes the paper.

II. SOSM Control

Fig. 1 shows the synchronous buck dc–dc converter, where V_g is the input voltage, v_o is the output voltage, i_L is the inductor current, R is the converter load, and L and C are the filter inductor and capacitor, respectively. The converter can be described by

$$\begin{aligned} \dot{v}_o &= -\frac{v_o}{CR} + \frac{i_L}{C} \\ \dot{i}_L &= -\frac{v_o}{L} + \frac{uV_g}{L} \end{aligned} \tag{1}$$

where $u \in \{0, 1\}$ is the control input. As usual, the control objective is to regulate the output voltage v_o to a desired reference voltage $V_{\rm ref}$. It is desired to maintain output voltage regulation in the presence of parameter uncertainties and load disturbances, and to do so without the need to sense currents.

The difference between the output voltage and the reference voltage is defined as the sliding variable s

$$s = v_o - V_{\rm ref}. \tag{2}$$

Considering a constant $V_{\rm ref}$, the first derivative of s can be found as

$$\dot{s} = -\frac{v_o}{CR} + \frac{i_L}{C} \tag{3}$$

and the second derivative of s as

$$\ddot{s} = \left[\frac{1}{(CR)^2} - \frac{1}{LC}\right] v_o - \frac{i_L}{C^2 R} + \frac{uV_g}{LC}. \tag{4}$$

The relative degree [16] of the sliding dynamics (4) for synchronous buck dc–dc converters is two. For the sliding dynamics (4), the combination of s and $\dot{s}$, e.g., $ks + \dot{s} = 0$ (k is a constant), is usually chosen to construct the sliding surface using traditional first-order SMC. A controller needs the knowledge of s and $\dot{s}$ in order to reach the sliding surface. Sensing the capacitor current is commonly employed to obtain $\dot{s}$. In contrast, in SOSM control, the sliding surface is chosen as $\{s = 0, \dot{s} = 0\}$. Note that expression (3) implies that the average value of the inductor current approaches the load current v_0/R as $\dot{s}$ converges to zero. This means that the output voltage can track the reference voltage and the average value of the inductor current can track the output current if the trajectory of sliding dynamics (4) is kept on the second-order sliding surface $\{s = 0, \dot{s} = 0\}$. Hence, the SOSM controller can regulate the output voltage to the reference value without sensing the current, if it can force both s and $\dot{s}$ to zero without measurement of $\dot{s}$. The SOSM control is based on this idea.

The main SOSM approaches include twist [21], supertwist [21], suboptimal [22] and improved suboptimal [20] algorithms. The advantage of the improved suboptimal algorithm [20] is that it allows the system to reach the nominal operating point without overshoot and without measurement of $\dot{s}$. In this paper, a SOSM controller based on the improved suboptimal algorithm is presented for synchronous dc–dc buck converters.

III. State-Machine Realization of SOSM Control

The state-machine controller presented in this section uses the sliding variable s, which is based on the improved suboptimal algorithm [20], steers the system trajectory to the switching surface $\{s = 0, \dot{s} = 0\}$ in spite of parameter uncertainties or load disturbances. The controller operation is presented in a general manner in this section first, and more specifically for the synchronous buck converter in Section IV.

The controller state-machine structure is shown in Fig. 2. It consists of four states named $A^+_{\rm OFF}, A^-_{\rm OFF}, A^+_{\rm ON}, A^-_{\rm ON}$, in addition to an initial state. The states $A^+_{\rm OFF}$ and $A^+_{\rm ON}$ are associated with the sliding variable $s \geq 0$, whereas the states $A^-_{\rm OFF}$ and $A^-_{\rm ON}$ correspond to the sliding variable $s < 0$. The states $A^+_{\rm OFF}$ and $A^-_{\rm OFF}$ are associated with trajectories when $\dot{s}$ is decreasing, while the states $A^+_{\rm ON}$ and $A^-_{\rm ON}$ correspond to trajectories when $\dot{s}$ is increasing. In each state, the corresponding control input

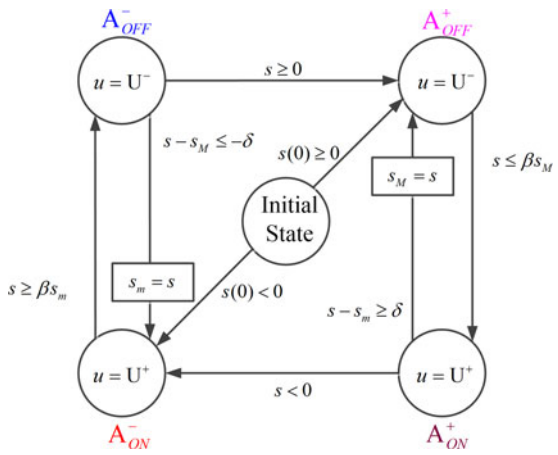

Fig. 2. State-machine controller based on the improved suboptimal algorithm [20].

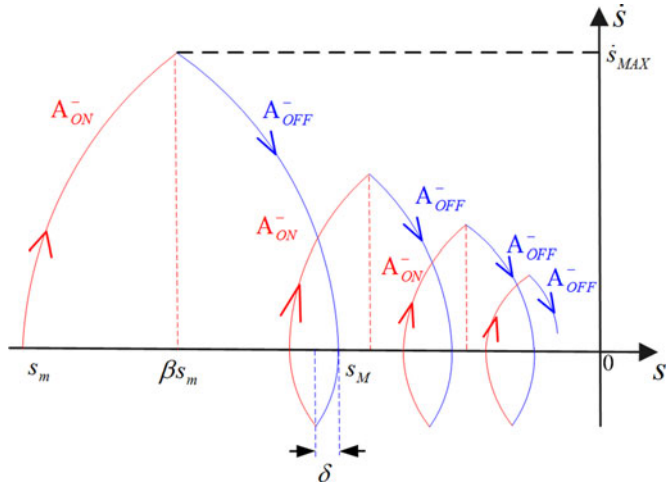

Fig. 3. Trajectory movement starting on the left-hand side of the $s - \dot{s}$ state plane.

is $U^+ = 1\,(ON)$ or $U^- = 0\,(OFF)$ as shown in Fig. 2. "ON" means ON state corresponding to position "1" of the switch in Fig. 1. "OFF" means OFF state corresponding to position "0" of the switch in Fig. 1.

The state machine controller steers the trajectory movement in the $s - \dot{s}$ state plane as shown in Figs. 3 and 4. The trajectory on the left-hand side of the state plane ($s < 0$) is driven by states $A^-_{\rm ON}$ and $A^-_{\rm OFF}$ as shown in Fig. 3. The trajectory on the right-hand side of the state plane ($s > 0$) is driven by states $A^+_{\rm OFF}$ and $A^+_{\rm ON}$ as shown in Fig. 4.

The state machine illustrated in Fig. 2 uses two additional variables, namely s_m and s_M. Variable s_m keeps the minimum value of s in the states $A^+_{\rm ON}$ and $A^-_{\rm ON}$, while variable s_M keeps the maximum value of s in the states $A^+_{\rm OFF}$ and $A^-_{\rm OFF}$. The switching conditions are determined by the variable s_m or s_M, which are updated with the change of the state.

In Fig. 3, variable s_m keeps the minimum value of s at the start of state $A^-_{\rm ON}$. The state $A^-_{\rm OFF}$ is then entered when the condition $\beta s_m (0 < \beta < 1)$ is satisfied, which implies that the point βs_m is closer to the origin than the point s_m. In state $A^-_{\rm OFF}$,

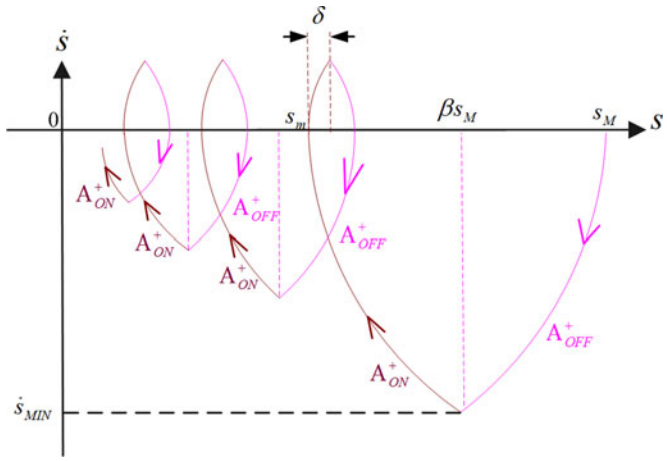

Fig. 4. Trajectory movement starting on the right-hand side of the $s - \dot{s}$ state plane.

the trajectory is approaching the horizontal axis. Variable s_M is updated to the new maximum value of s at the point when the trajectory crosses the horizontal axis in state $A^-_{\rm OFF}$. The trajectory then moves away from the horizontal axis until the condition $s_M - s > \delta$ is satisfied. Here, δ is a hysteresis parameter, which ensures that the switching frequency is bounded to a desired value, as discussed further in Section IV-B. Once the trajectory crosses the hysteresis threshold, state $A^-_{\rm ON}$ is activated again. Variable s_m keeps the new minimum value of s when the trajectory crosses the horizontal axis in state $A^-_{\rm ON}$, and the process proceeds iteratively as described above. If δ is small enough, the trajectory converges to the vicinity of the origin in the $s - \dot{s}$ plane as shown in Fig. 3. The trajectory starting on the right-hand side of the $s - \dot{s}$ plane has a similar behavior as shown in Fig. 4.

The sliding-mode variable of the controlled system is closer to the origin in each cycle. It should be noted that the value of β must be constrained in order to prevent the trajectory from crossing the vertical axis, which would result in undesirable overshoots or instability.

Similar to the improved suboptimal algorithm described in [20], measurement of $\dot{s}$ is not required. The sign of $\dot{s}$ is detected by means of the aforementioned hysteretic method.

In the next section, the proposed control strategy is developed for synchronous buck dc–dc converters, including derivation of β to ensure stability and fast response, and hysteresis δ to limit the switching frequency.

IV. State-Machine Controller Analysis and Design

A. Analysis of Transient for a Synchronous Buck Converter

According to expression (4), the second derivative of the sliding variable s can be expressed as

$$\ddot{s} + \frac{1}{RC}\dot{s} + \frac{1}{LC}s = \frac{uV_g - V_{\rm ref}}{LC}. \tag{5}$$

Given that load R is in the range $(0, \infty]$, (5) corresponds to the dynamics of a damped oscillator with an equilibrium point at $s = -V_{\rm ref}$ when $u = 0$ and at $s = V_g - V_{\rm ref}$ when $u = 1$.

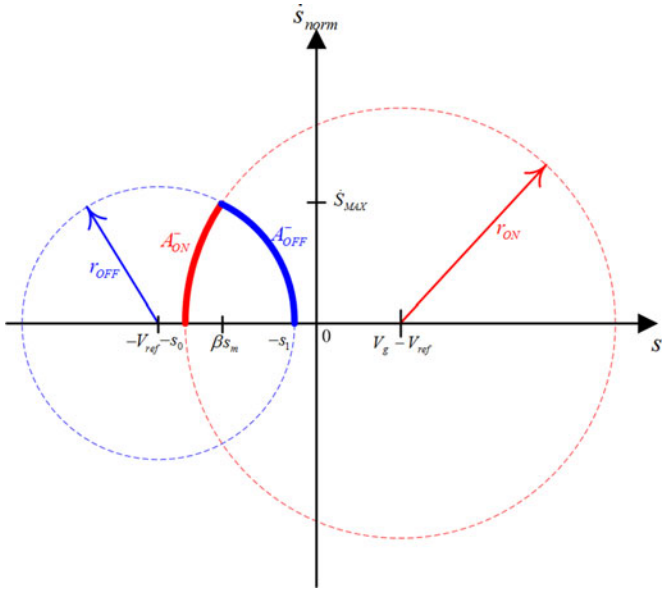

Fig. 5. Undamped state-plane trajectory starting at $(-s_0, 0)$.

It is convenient to consider undamped dynamics, i.e., the case when the converter is unloaded. Equation (5) can be expressed as

$$\ddot{s} + \frac{1}{LC} s = \frac{u V_g - V_{\text{ref}}}{LC}. \tag{6}$$

Under the normalization $\dot{s}_{\text{norm}} = \sqrt{LC}\dot{s}$, the ON state behavior can be represented as

$$\sqrt{LC}\ddot{s}_{\text{norm}} + s = V_g - V_{\text{ref}}. \tag{7}$$

The state-plane trajectory is described by a circle

$$\dot{s}_{\text{norm}}^2 + \left(s - (V_g - V_{\text{ref}})\right)^2 = r_{\text{ON}}^2 \tag{8}$$

where the circle radius r_{ON} depends on the initial conditions as shown in Fig. 5. The state-plane trajectory, starting from an initial point $(-s_0, 0)$, $s_0 > 0$ on the left-hand side of the state plane, evolves along the state circle

$$\dot{s}_{\text{norm}}^2 + \left(s - (V_g - V_{\text{ref}})\right)^2 = \left(s_m - (V_g - V_{\text{ref}})\right)^2. \tag{9}$$

Note that variable s_m keeps the value of $-s_0$ as described in Section III. The trajectory moves along the circle until $s = \beta\, s_m$, where

$$\left(\beta s_m - (V_g - V_{\text{ref}})\right)^2 + \dot{s}_{\text{MAX}}^2 = \left(s_m - (V_g - V_{\text{ref}})\right)^2 \tag{10}$$

and $\dot{s}_{\text{MAX}}$ is the largest value of $\dot{s}_{\text{norm}}$. After passing the point $(\beta s_m, \dot{s}_{\text{MAX}})$, the trajectory follows the OFF state circle:

$$\left(s + V_{\text{ref}}\right)^2 + \dot{s}_{\text{norm}}^2 = r_{\text{OFF}}^2 \tag{11}$$

until it crosses the horizontal axis at point $(-s_1, 0)$, $s_1 > 0$ that satisfies the following condition:

$$\left(s_M + V_{\text{ref}}\right)^2 = r_{\text{OFF}}^2. \tag{12}$$

Note that variable s_M keeps the value of $-s_1$ as described in Section III. Considering the intersection point $(\beta s_m, \dot{s}_{\text{MAX}})$ of arc A_{ON}^{-} and A_{OFF}^{-} from (10)–(12), the following equation holds:

$$\begin{aligned}\left(s_M + V_{\text{ref}}\right)^2 \;=\; & \left(\beta\, s_m + V_{\text{ref}}\right)^2 + \left(s_m - (V_g - V_{\text{ref}})\right)^2 \\ & - \left(\beta\, s_m - (V_g - V_{\text{ref}})\right)^2. \end{aligned} \tag{13}$$

In order to prevent an overshoot of the output voltage, the trajectory should not cross the vertical axis, which means that the condition $-s_1 \le 0$ should be fulfilled. Hence, β should be greater than $\beta_{N\,\min}$, which is the value that brings the trajectory to the origin for a negative value of s. From (13), with $s_1 = 0$, the minimum β in the operating range $[-V_{\text{ref}}, 0]$ can be found as

$$\beta_{N\,\min} = 1 + \frac{-s_m - 2V_{\text{ref}}}{2V_g}. \tag{14}$$

Considering the worst case when the output voltage starts from zero, $s_m = -V_{\text{ref}}$, a condition for parameter β to ensure that the trajectory does not cross the vertical axis follows from (14):

$$\beta_N \ge 1 - \frac{V_{\text{ref}}}{2V_g}. \tag{15}$$

The analysis above has been done considering an undamped trajectory, which in fact implies that condition (15) guarantees that no damped trajectory would cross the vertical axis, because damped trajectories move along converging spirals bounded by the considered circles.

Taking (10) into account, the following relationship can be found:

$$\dot{s}_{\text{MAX}}^2 = \left(1 - \beta^2\right) s_m^2 - 2\left(1 - \beta\right)\left(V_g - V_{\text{ref}}\right) s_m \tag{16}$$

which implies that as the sequence s_m tends to the origin under the conditions of (14) or (15), the sequence of maximal values $\dot{s}_{\text{MAX}}$ in the vertical axis also tends to the origin. The fact that both sequences are contractive proves stability of the control approach for any initial point in the left-hand side of the state plane.

The same analysis can be done for a point starting from the right-hand side of the state plane as shown in Fig. 6. For this case, a constraint for β can be found as

$$\beta_{P\,\min} = \frac{1}{2}\frac{s_M + 2V_{\text{ref}}}{V_g}. \tag{17}$$

Considering the starting point $(V_g - V_{\text{ref}}, 0)$ in the operating range $[0, V_g - V_{\text{ref}}]$, β in the proposed control approach may be chosen according to

$$\beta_P \ge \frac{1}{2}\left(1 + \frac{V_{\text{ref}}}{V_g}\right). \tag{18}$$

Similar to (16), the following equation holds:

$$\dot{s}_{\text{MIN}}^2 = \left(1 - \beta^2\right) s_M^2 + 2\left(1 - \beta\right) V_{\text{ref}}\, s_M \tag{19}$$

which also implies that as the sequence s_M tends to the origin under the conditions of (17) or (18), the sequence of minimal values $\dot{s}_{\text{MIN}}$ also tends to the origin. That means that both sequences are contractive, which proves stability of the control

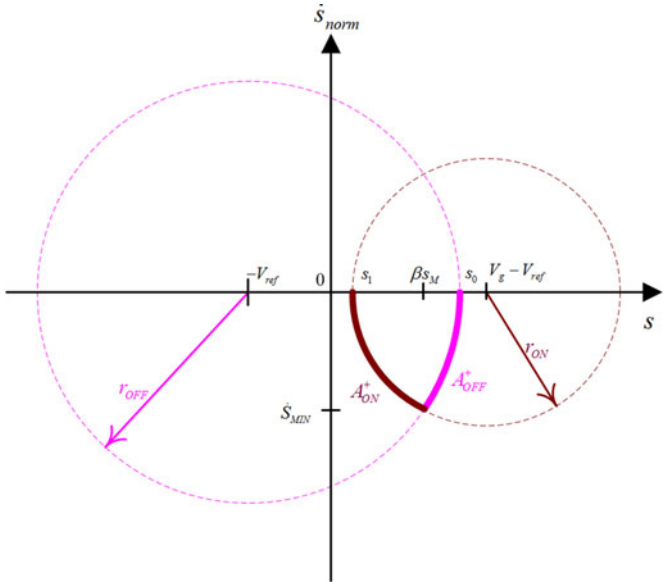

Fig. 6. Undamped state-plane trajectory starting at $(s_0, 0)$.

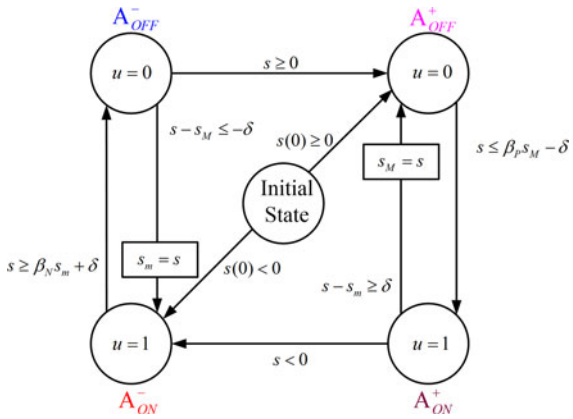

Fig. 7. Controller state-machine diagram including hysteresis.

method for a point starting on the right-hand side of the state plane.

B. Behavior Around the Equilibrium and Determination of Hysteresis

If hysteresis δ trends to zero, a controller operating according to the state machine diagram in Fig. 2 would theoretically result in infinite switching frequency as the converter approaches the equilibrium. A finite-frequency steady-state operation can be obtained after left the starting point, using the hysteresis parameter δ in the controller state machine diagram shown in Fig. 7. Steady-state operation is examined in this section first for the case when the controller operates with constant parameters β_N and β_P, and then, for the case when these parameters are adaptively adjusted during controller operation.

1) Controller Implementation With Constant Parameters β_N and β_P: If parameter β is chosen according to (15) (when the operating point is in the left half of the state plane) or according

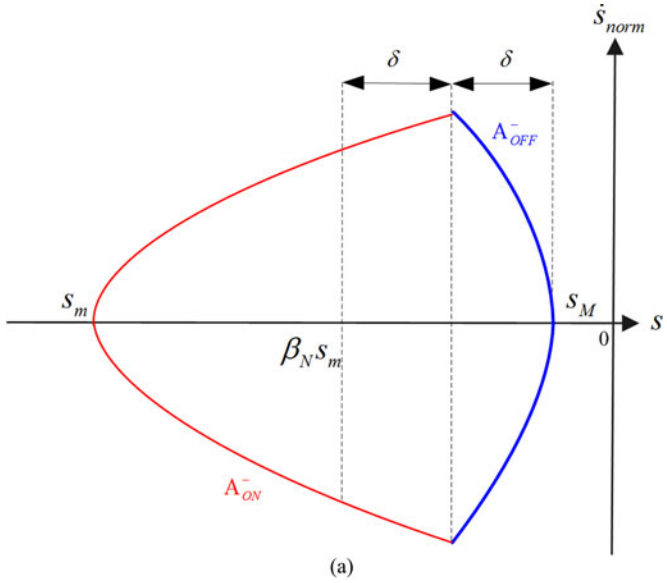

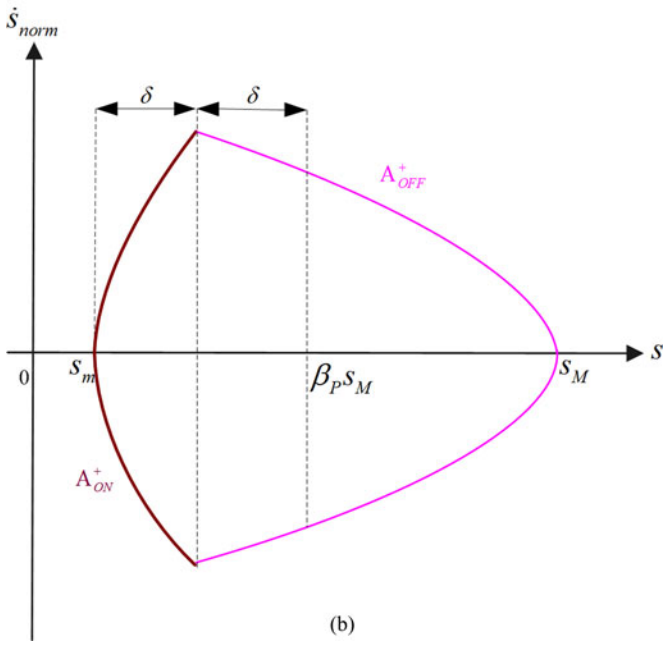

Fig. 8. Steady-state trajectories for (a) $V_{\rm ref} > \frac{2}{3}\left(2V_g - \sqrt{-6\delta V_g + V_g^2}\right)$ and (b) $V_{\rm ref} < \frac{1}{3}\left(-V_g + 2\sqrt{-6\delta V_g + V_g^2}\right)$ when β_N and β_P chosen according to (15) and (18), respectively, are constant.

to (18) (when the operating point in the right half of the state plan), a dc error appears in the steady-state operation. This is because the trajectory goes into a steady-state limit cycling before arriving at the origin in the $s - \dot{s}_{\rm norm}$ state plane as shown in Fig. 8. The following conditions must be hold for limit cycling:

$$\beta_N s_m + \delta = s_M - \delta, \quad \left(V_{\rm ref} > \frac{V_g}{2}\right) \tag{20}$$

$$s_m + \delta = \beta_P s_M - \delta, \quad \left(V_{\rm ref} < \frac{V_g}{2}\right). \tag{21}$$

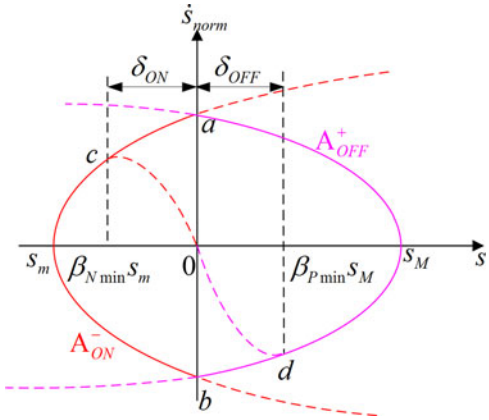

Fig. 9. State-plane trajectory around the origin when the converter is unloaded.

If β_N and β_P are chosen according to (15) and (18) immutable, in order to fulfill the conditions for limit cycling, the results in equilibrium can be expressed as

$$s_M = 2\delta + \left(1 - \frac{V_{\rm ref}}{2V_g}\right) s_m \le 0, \quad \left(V_{\rm ref} \ge \frac{2}{3}\left(2V_g - \sqrt{-6\delta V_g + V_g^2}\right) \approx \frac{2V_g}{3}\right) \tag{22}$$

$$s_m = \frac{V_g + V_{\rm ref}}{2V_g} s_M - 2\delta \ge 0, \quad \left(V_{\rm ref} \le \frac{1}{3}\left(-V_g + 2\sqrt{-6\delta V_g + V_g^2}\right) \approx \frac{V_g}{3}\right). \tag{23}$$

It should be noted that results (22) and (23) can be fulfilled for any δ when the trajectory is near the origin. However, the trajectory stays around the origin accurately only when $V_{\rm ref} = V_g/2$. Alternative approaches based on adaptively adjusting values of parameter β in order to reduce the steady-state error are considered next.

2) Implementation With Various Parameters β_N and β_P: Considering that $s_M/2V_g \approx 0$ and $s_m/2V_g \approx 0$ in steady state, let parameter $\beta_{N\min} = 1 - \frac{V_{\rm ref}}{V_g}$ when $V_{\rm ref} > V_g/2$ and $\beta_{P\min} = \frac{V_{\rm ref}}{V_g}$ when $V_{\rm ref} < V_g/2$ after the trajectory goes into steady state. With this approach, the trajectory is forced to cross the vertical axis in steady state and stay around the origin. However, it should be noted that the equilibrium moves slightly around the origin when the load is changed.

Parameter β_N is updated at the transitions from $A^-_{\rm OFF}$ to $A^-_{\rm ON}$ and from $A^-_{\rm OFF}$ to $A^+_{\rm OFF}$. Parameter β_P is updated at the transitions from $A^+_{\rm ON}$ to $A^+_{\rm OFF}$ and from $A^+_{\rm ON}$ to $A^-_{\rm ON}$. With the proposed approach of dynamically adjusted β, the trajectory goes into a limit cycle around the origin as shown in Fig. 9. The maximum and the minimum values of the trajectory are independent of the inductance and capacitance values.

Fig. 9 shows the hysteresis $\delta_{\rm ON}$ in ON mode and $\delta_{\rm OFF}$ in OFF mode. It can be shown that $\delta_{\rm ON} = \delta_{\rm OFF}$ as follows. Points c and d correspond to the switching points without hysteresis from $A^-_{\rm ON}$ to $A^-_{\rm OFF}$ and from $A^+_{\rm OFF}$ to $A^+_{\rm ON}$ in Fig. 7, respectively. When hysteresis is applied, assuming both switching points in a period are at the vertical axis, the switching conditions are changed to be as follows, respectively:

$$s \ge \beta_{N\min} s_m + \delta_{\rm ON} = 0 \tag{24}$$

$$s \le \beta_{P\min} s_M - \delta_{\rm OFF} = 0 \tag{25}$$

with the switching points denoted as points a and b in Fig. 9.

Considering (14), (17), (24), and (25), the hysteresis values can be expressed as

$$\delta_{\rm ON} = -\left(1 + \frac{-s_m - 2V_{\rm ref}}{2V_g}\right) s_m = \frac{s_m^2 - 2V_g s_m + 2V_{\rm ref} s_m}{2V_g} \tag{26}$$

$$\delta_{\rm OFF} = \frac{s_M + 2V_{\rm ref}}{2V_g} s_M = \frac{s_M^2 + 2V_{\rm ref} s_M}{2V_g}. \tag{27}$$

The switching point a and b are symmetrical about the horizontal axis, where the following equations hold:

$$(V_g - V_{\rm ref})^2 + \dot{s}_{\rm MAX}^2 = (s_m - (V_g - V_{\rm ref}))^2 \tag{28}$$

$$V_{\rm ref}^2 + (-\dot{s}_{\rm MAX})^2 = (s_M + V_{\rm ref})^2. \tag{29}$$

Then,

$$s_m^2 - 2V_g s_m + 2V_{\rm ref} s_m = s_M^2 + 2V_{\rm ref} s_M. \tag{30}$$

Considering (26), (27), and (30), the following relation is obtained:

$$\delta_{\rm ON} = \delta_{\rm OFF} \tag{31}$$

According to (31), if the same hysteresis is set for ON mode and OFF mode, the switching happens at the vertical axis ($s = 0$) in every period. Both switching points move slightly in the opposite directions when the load resistance varies. Otherwise, the line connecting the switching points intersects the origin state as shown in Fig. 10. Hence, the limit cycle of the output voltage is still fixed at the origin in the state plane $s - \dot{s}_{\rm norm}$.

Considering (14), (17), (24), and (25), the voltage ripple without load is

$$\delta_v = |s_m| + |s_M| = \frac{\delta}{\beta_N} + \frac{\delta}{\beta_P} = \frac{\delta V_g}{V_g - V_{\rm ref}} + \frac{\delta V_g}{V_{\rm ref}} \tag{32}$$

where δ is the hysteresis, $\frac{s_m}{2V_g} \approx 0$, $\frac{s_M}{2V_g} \approx 0$. Equation (32) implies that the output ripple is independent of filter inductance or capacitance values.

Considering (5), if the trajectory is close enough to the origin, where $|s| << V_g - V_{\rm ref}$ and $|\dot{s}| << (V_g - V_{\rm ref})\frac{R}{L}$, the converter dynamics can be approximated by

$$\ddot{s} = \frac{uV_g - V_{\rm ref}}{LC}. \tag{33}$$

Thus, the solution of (33) can be expressed as

$$s(t) = \left(\frac{uV_g - V_{\rm ref}}{LC}\right)\frac{t^2}{2} + \dot{s}(0)t + s(0). \tag{34}$$

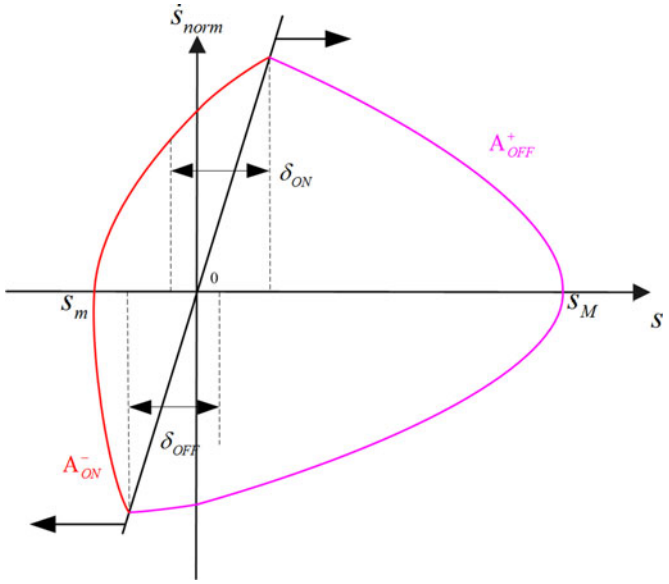

Fig. 10. State-plane trajectory around the origin when the converter is loaded.

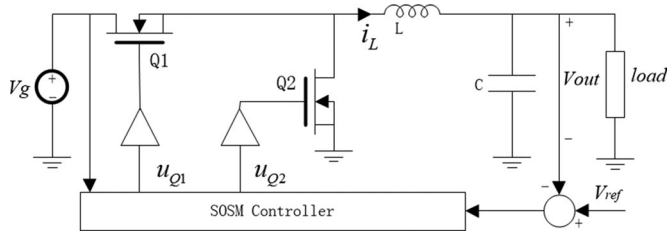

Fig. 11. Synchronous buck converter with SOSM controller.

TABLE I
SYNCHRONOUS BUCK CONVERTER PARAMETERS

Parameter	Value
C	$270\ \mu$F
L	$1.26\ \mu$H
$V_{\rm ref}$	1.25 V
R	$0.125 - 0.5\ \Omega$
V_g	$5 - 10$ V
$R_{\rm inductor} + R_{\rm on}$	$20\ \text{m}\Omega$
$R_{\rm ESR}$	$< 0.7\ \text{m}\Omega$

Considering that the point is near the equilibrium as shown in Fig. 9, which means $\dot{s}(0)\, t \approx 0$ in a period, the time t_{s_m} of ON modes starting from s_m to the next switching point a in the limit cycle fulfills

$$t_{s_m} = \sqrt{\frac{2LC\,|s_m|}{V_g - V_{\rm ref}}} = \sqrt{-\frac{2LC\delta}{(V_g - V_{\rm ref})\,\beta_N}} = \frac{1}{V_g - V_{\rm ref}}\sqrt{2LC\delta V_g} \tag{35}$$

and the time t_{S_M} of OFF modes starting from s_M to the next switching point b in the limit cycle fulfills

$$t_{S_M} = \sqrt{\frac{2LC\,|s_M|}{V_{\rm ref}}} = \sqrt{\frac{2LC\delta}{V_{\rm ref}\beta_P}} = \frac{1}{V_{\rm ref}}\sqrt{2LC\delta V_g}. \tag{36}$$

The switching period is

$$T = 2\,(t_{s_m} + t_{S_M}) = 2\sqrt{2LC\delta V_g}\,\frac{V_g}{(V_g - V_{\rm ref})\,V_{\rm ref}}. \tag{37}$$

Equation (37) implies that the switching frequency is affected by filter inductance or capacitance values. It should be noted that the voltage ripple (32) and the switching period (37) are derived for the undumped case. Considering the load and the parasitic elements in the converter, the trajectory in steady state is as shown in Fig. 10. The actual voltage ripple is smaller than the one obtained from (32), and the switching period is shorter than the one calculated from (37), because some energy is dissipated on the load and the parasitic elements.

V. Experimental Verification

In this section, the proposed control is verified on a 1.25-V 10-A synchronous buck converter supplied from $V_g = 5$ V to $V_g = 10$ V as shown in Fig. 11 and Table I. Some implementation issues are addressed and experimental results are provided to verify performance of the proposed controller. The parameters of the synchronous buck converter prototype are listed in Table I.

The controller has been implemented in an Altera Cyclone III FPGA with a 30-MHz clock frequency. An A/D converter with 30 MHz, 11 bits, and 0–2 V input range has been used to measure the output voltage. The A/D LSB resolution is $q_{\rm A/D} = 2\ \text{V}/2048 \approx 1\ \text{mV}$. The time delay of the A/D converter is five clocks. The time delay from FPGA to the switches is three clocks because a multiplier and a divider are used to calculate some firing conditions. The total time delay is 267 ns, which may result in slightly larger ripple and longer switching period compared to the values calculated by (32) and (37), respectively, but the delay does not affect stability of the proposed control approach. The deadtime for the synchronous switches is approximately 350 ns.

As discussed above, parameter β depends on the input voltage. In order to implement this dependence, a low resolution A/D converter is sufficient for sensing the input voltage. The speed of this additional A/D converter can be chosen depending on the expected input voltage dynamics. In the experimental results reported in this paper, the input voltage dependence is implemented and verified by manual adjustments of parameter β.

Although the proposed control approach can be implemented by means of discrete circuit elements or relatively simple custom logic, an FPGA is used to simplify prototyping and to allow flexible experimentations with various parameters such as $\beta_{N\,\min}$ and $\beta_{P\,\min}$. The capacitor equivalent series resistance, switch ON resistance, the inductor series resistance, and other parasitic elements add some additional terms in the $\dot{s}$ and $\ddot{s}$ expressions. In the prototype presented in this paper, these effects can be considered relatively small and are neglected. A detailed treat-

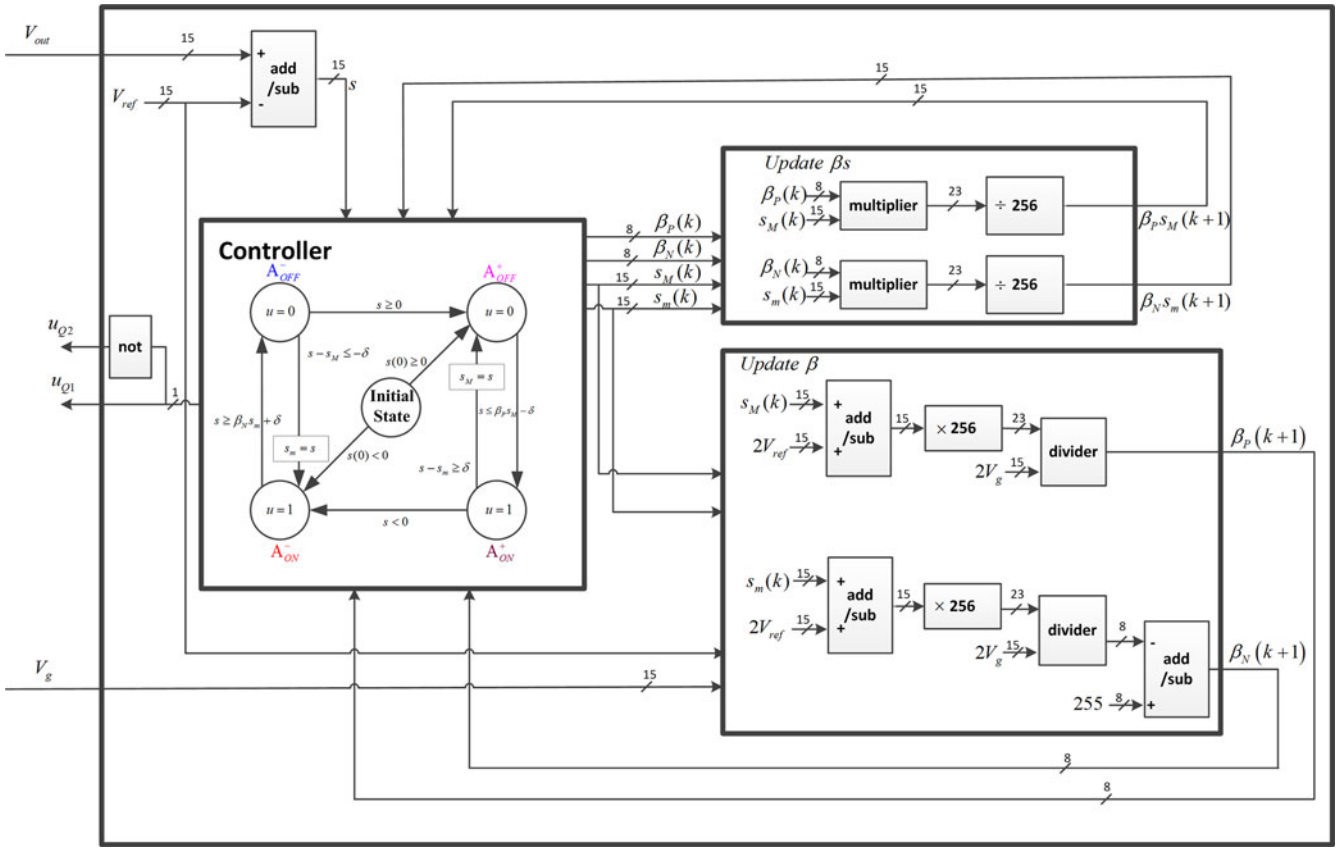

Fig. 12. Block diagram of the FPGA implementation of the proposed controller.

ment of the SOSM control approach taking into account various parasitic elements can be found in [24]. An application to a higher order converter system has been presented in [25].

The controller is implemented as a state machine with four states and an initial state as shown in Fig. 12. The multipliers, adders, and dividers are implemented using Altera's Library of Parameterized Modules. In order to store a decimal with a register on the FPGA, the parameter β is scaled with the scaling factor 256 times due to $\beta \in (0, 1)$. Two 8-bit registers are used to store the parameter β_P and β_N. Calculations include two parts: βs and β. The value of $\beta_P s_M(k+1)$ is used in the transition condition from state $A^+_{\rm OFF}$ to state $A^+_{\rm ON}$, and the value of $\beta_N s_m(k+1)$ is used in the transition condition from state $A^-_{\rm ON}$ to state $A^-_{\rm OFF}$. The update of β depends on s_M or s_m in the controller with adjustable β.

In the following sections, experimental results are presented for the start-up, step-up, and step-down transients. The performances are compared for two cases related to how parameter β is handled, an implementation with constant β and an implementation with adjustable β.

A. Implementation With Constant β

As discussed above, $\beta_N = 0.875$, which is the minimum in (15) and $\beta_P = 0.25$, which is chosen by (17) at $s_M = 0$ because $V_{\rm ref} < \frac{V_g}{2}$. Hysteresis δ is chosen to be 6 mV. Fig. 13 compares start-up transients of the proposed controller for 0–5

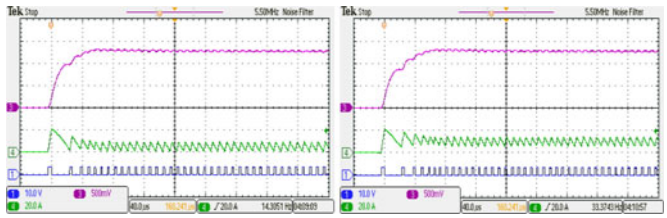

Fig. 13. Experimental start-up transient waveforms with $V = 5$ V and the constant β method; $\beta_N = 0.875$ and $\beta_P = 0.25$ .The transients are shown for 5- (left) and 10-A (right) load. The signals shown, top to bottom, are the output voltage, inductor current, and switch control signal.

and 0–10 A with 5-V input voltage. The start-up transient lasts several switching periods because of the energy dissipated by the parasitic elements and the load. The number of switching periods during transient increases with increasing of the output current. In all cases, the output voltage approaches steady state regulation without any overshoots.

Fig. 14 illustrates dynamic responses for 0–5- and 0–10-A step-up load transients. The waveforms are shown for the worst-case conditions corresponding to the cases when the step load occurs at the minimum output voltage. The output voltage returns to the reference after just two switching periods for the 0–5-A load transient, and after just three switching periods for the 0–10-A load transient. The steady-state voltage ripple is about 40 mV, and the switching period is about 9 μs. It should be noted that the output voltage ripple become slightly smaller

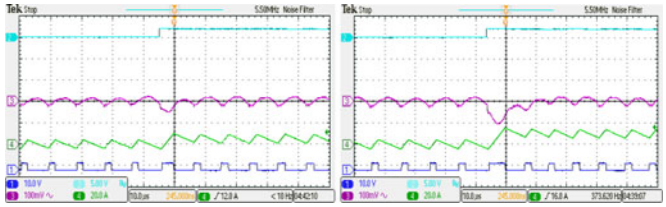

Fig. 14. Experimental step-up load transients with $V_g = 5$ V and the constant β method; $\beta_N = 0.875$ and $\beta_P = 0.25$. The load transients are 0–5 (left) and 0–10 A (right). The signals, top to bottom, are the load change signal, the output voltage, inductor current, and the switch control signal.

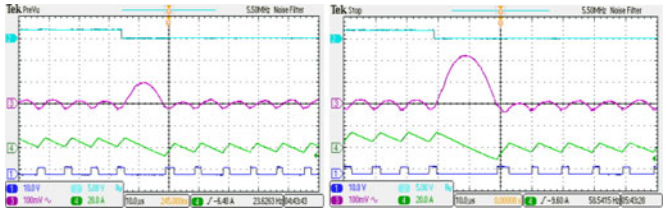

Fig. 15. Experimental step-down load transients with $V_g = 5$ V and the constant β method; $\beta_N = 0.875$ and $\beta_P = 0.25$. The transients are 5–0 (left) and 10–0 A (right). The signals, top to bottom, are: the load change signal, the output voltage, inductor current and switch control signal.

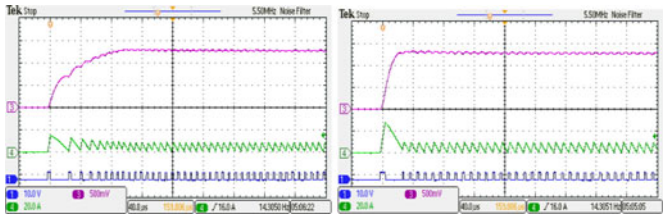

Fig. 16. Experimental start-up transient waveforms for $\beta_N = 0.95$ (left) and $\beta_N = 0.78$ (right), with constant $\beta_P = 0.25$, $R = 0.25$, and $V_g = 5$ V.

at larger output currents. This is because of the shift in the switching point, as discussed in Section III.

Fig. 15 illustrates dynamic responses with the proposed controller for 5–0- and 10–0-A step-down load transients. With the proposed controller, the converter returns to regulation after one switching period, which is because β_P is chosen according to (17) when $V_{\rm ref} < \frac{V_g}{2}$ assuming $\frac{s_M}{2V_g} \approx 0$ in steady state. The output voltage is forced to cross the reference level.

It is instructive to examine the controller responses for different values of the parameter β_N. Fig. 16 illustrates the start-up transient waveforms for two different values, $\beta_N = 0.95$ and $\beta_N = 0.78$, with constant $\beta_P = 0.25$, $R = 0.25$, and $V_g = 5$ V. The scenario illustrates how the peak inductor current during a start-up transient may be limited (at the expense of longer transient) by increasing the parameter β_N. The second scenario illustrates how a time-optimal transient [3], [4] may be achieved by decreasing β_N to a selected value for this particular operating point.

B. Implementation With Adjustable β

Start-up transients with the adjustable β method are shown in Fig. 17. In this case, $\beta_N = 0.875$ and $\beta_P = 0.625$ at the starting

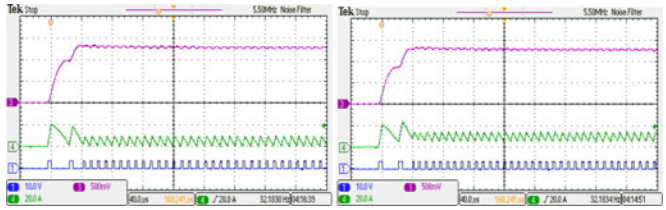

Fig. 17. Experimental start-up transient waveforms with $V_g = 5$ V and the adjustable β method. The transients are at 5-A load (left) and at 10- A load (right). The signals, top to bottom, are the output voltage, inductor current, and the switch control signal.

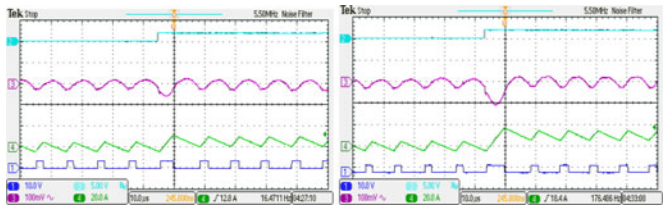

Fig. 18. Experimental step-up load transient waveforms with $V_g = 5$ V and the adjustable β method. The transients are 0–5 (left) and 0–10 A (right). The signals are, top to bottom, load change signal, output voltage, inductor current, and switch control signal.

point, corresponding to the minimum values in (15) and (18), respectively. The parameter β_N is then updated using (14) and β_P is updated using (17). The experimental results show how the transients are faster compared to the constant β implementation. The output voltage reaches the reference voltage after only two switching periods.

Fig. 18 illustrates step-up transient waveforms with the proposed controller for 0–5- and 0–10-A load transients, under the worst-case conditions. As in ideal time-optimal responses, the output voltage goes back to regulation after only one switching period in both cases. The steady-state voltage ripple is 50 mV, and the switching period is 10 μs. These values are slightly larger than the voltage ripple of 32 mV obtained from (32) and the switching period of 9.6 μs from (37), respectively, because of time delay effects. It should also be noted that the output voltage ripple and the switching period are slightly larger compared to the constant β method. This is because the switching point is closer to the reference voltage when the output voltage is less than the reference voltage in the adjustable β method, which makes the output voltage deviate further away after crossing the reference voltage.

Fig. 19 illustrates step-down dynamic responses for 5–0- and 10–0-A load transients. The proposed controller achieves regulation in just one switching period, which is the same as with the constant β method.

Experimentally measured state-plane trajectories during start-up and step-load transients are shown in Figs. 20 and 21, respectively. The controller achieves a start-up response with just two switching actions and a step-load response with just one switching action.

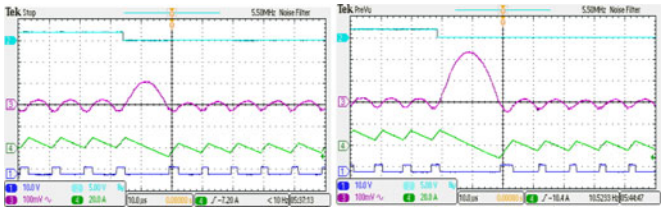

Fig. 19. Experimental step-down waveforms with $V_g = 5\text{V}$ and the adjustable β method. The load transients are 5–0 A (left) and 10–0 A (right). The signals, top to bottom, are load change signal, output voltage, inductor current, and switch control signal.

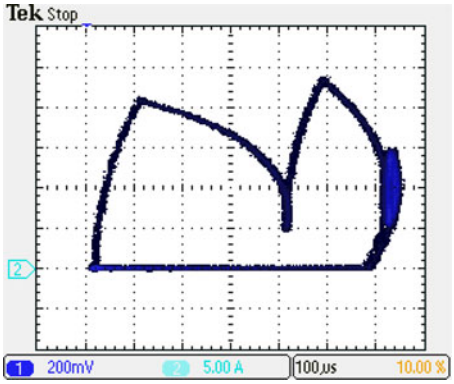

Fig. 20. State-plane trajectory during start-up transient experiment in the output voltage versus inductor current state plane with $V_g = 5$ V and using the adjustable β method, the horizontal axis is the output voltage and the vertical axis is the inductor current.

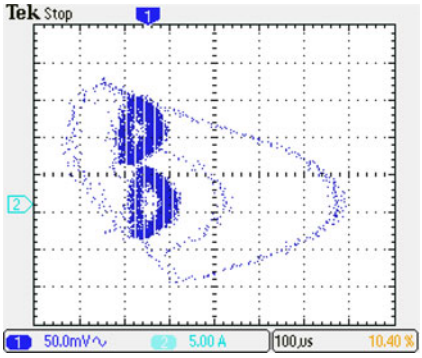

Fig. 21. State-plane trajectory during step-up and step-down load transient experiments in the output voltage versus inductor current state plane with $V_g = 5$ V and using the adjustable β method, the horizontal axis is the output voltage (ac coupled) and the vertical axis is the inductor current.

C. Transient Responses for Different Input Voltages

In order to test the performance at different input voltages, a start-up transient with $V_g = 10\text{V}$ is considered. In this case, $\beta_N = 0.9375$, which is the minimum from (15), and $\beta_P = 0.125$, which is chosen according to (17) at $s_M = 0$ because $V_{\text{ref}} < \frac{V_g}{2}$ with the constant β implementation. For the higher input voltage case, the controller requires a faster and more precise voltage measurements because the output voltage changes faster during the ON state, and a sensing noise is more likely to affect switching transitions more significantly. In the prototype, $\delta = 7\,\text{mV}$ is chosen, while all other conditions for the A/D converter and the FPGA implementation are the same as in the $V_g = 5$ V case. Figs. 22 and 23 illustrate start-up transient waveforms for the constant β and the adjustable β methods, respectively, with $V_g = 10\,\text{V}$. One may observe that the start-up transient waveforms are similar to the ones observed at $V_g = 5\,\text{V}$. The steady-state voltage ripple is now about 100 mV and the switching period is about 13 μs, which are larger than 55 mV and 11.7 μs calculated from (32) and (37), respectively, because time delay effects are more significant given the higher voltage difference between the input voltage and the reference.

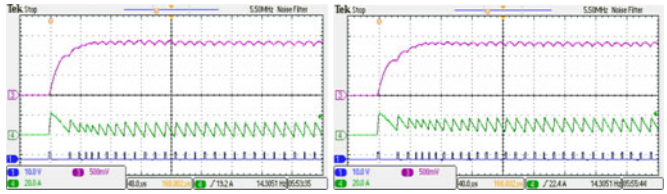

Fig. 22. Experimental start up transient waveforms with $V_g = 10$ V and the constant β method, $\beta_N = 0.9375$ and $\beta_P = 0.125$. The transients are at 5-A load (left) and at 10-A load (right). The signals, top to bottom, are output voltage, inductor current, and switch control signal.

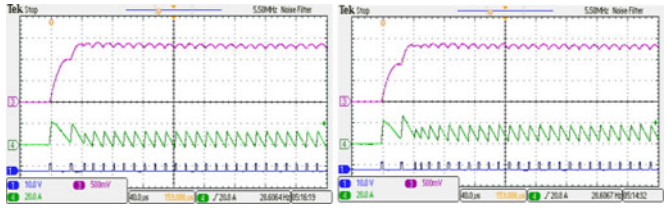

Fig. 23. Experimental start-up transient waveforms with $V_g = 10$ V and the adjustable β method. The transients are at 5-A load (left) and at 10-A load (right). The signals, top to bottom, are output voltage, inductor current, and switch control signal.

VI. Conclusion

A SOSM control method is described in this paper and applied to synchronous buck dc–dc converters. The proposed SOSM controller is implemented digitally in the form of a relatively simple state machine. The controller structure is described, together with state-plane analyses of transient and steady-state trajectories. A hysteresis method is introduced to control the steady-state switching frequency. By analysis and experiments, it is shown that the proposed SOSM controller can achieve stability, fast transient responses, and robust operation in the presence of load disturbances and parameter uncertainties. The approach does not require current sensing and does not rely on an integral term in the control loop. Experimental results verifying the controller performance are presented for a 1.25-V 10-A synchronous buck dc–dc converter.

References

[1] R. W. Erickson and D. Maksimovic, *Fundamentals of Power Electronics*, 2nd ed. New York, NY, USA: Springer-Verlag, 2001.

[2] R. D. Middlebrook and S. Cuk, "A general unified approach to modeling switching-converter power stages," in *Proc. IEEE Power Electron. Spec. Conf. Rec.*, 1976, pp. 18–34.

[3] A. Babazadeh and D. Maksimovic, "Hybrid digital adaptive control for fast transient response in synchronous buck DC-DC converters," *IEEE Trans. Power Electron.*, vol. 24, no. 11, pp. 2625–2638, Nov. 2009.
[4] V. Yousefzadeh, A. Babazadeh, B. Ramachandran, E. Alarcón, L. Pao, and D. Maksimović, "Proximate time-optimal digital control for synchronous buck DC-DC converters," *IEEE Trans. Power Electron.*, vol. 23, no. 4, pp. 2018–2026, Jul. 2008.
[5] K. K. S. Leung and H. S. H. Chung, "Derivation of a second-order switching surface in the boundary control of buck converters," *IEEE Power Electron. Lett.*, vol. 2, no. 2, pp. 63–67, Jun. 2004.
[6] M. Ordonez, M. T. Iqbal, and J. E. Quaicoe, "Selection of a curved switching surface for buck converters," *IEEE Trans. Power Electron.*, vol. 21, no. 4, pp. 1148–1153, Jul. 2006.
[7] G. E. Pitel and P. T. Krein, "Minimum-time transient recovery for DC-DC converters using raster control surfaces," *IEEE Trans. Power Electron.*, vol. 24, no. 12, pp. 2692–2703, Dec. 2009.
[8] R. Venkataramanan, A. Sabanovic, and S. Cuk, "Sliding mode control of DC-to-DC converters," in *Proc. IEEE Conf. Ind. Electron. Control Instrum.*, 1985, pp. 251–258.
[9] V. I. Utkin, *Sliding Modes in Control and Optimization*. New York, NY, USA: Springer-Verlag, 1992.
[10] R. Marino and P. Tomei, *Nonlinear Control Design*. London. U.K.: Prentice-Hall, 1995.
[11] H. Sira-Ramirez, "Sliding motions in bilinear switched networks," *IEEE Trans. Circuits Syst.*, vol. CS-34, no. 8, pp. 919–933, Aug. 1987.
[12] P. Mattavelli, L. Rossetto, and G. Spiazzi, "Small-signal analysis of DC-DC converters with sliding mode control," *IEEE Trans. Power Electron.*, vol. 12, no. 1, pp. 96–102, Jan. 1997.
[13] S. C. Tan, Y. M. Lai, and C. K. Tse, "General design issues of sliding-mode controllers in DC-DC converters," *IEEE Trans. Ind. Electron.*, vol. 55, no. 3, pp. 1160–1174, Mar. 2008.
[14] S. C. Tan, Y. M. Lai, M. K. H. Cheung, and C. K. Tse, "On the practical design of a sliding mode voltage controlled buck converter," *IEEE Trans. Power Electron.*, vol. 20, no. 2, pp. 425–437, Mar. 2005.
[15] S. K. Mazumder, A. H. Nayfeh, and A. Borojevic, "Robust control of parallel DC-DC buck converters by combining integral-variable-structure and multiple-sliding-surface control schemes," *IEEE Trans. Power Electron.*, vol. 17, no. 3, pp. 428–437, May 2002.
[16] H. K. Khalil, *Nonlinear Systems*. 3rd ed. Englewood Cliffs, NJ, USA: Prentice-Hall, 2001.
[17] E. Fossas and A. Ras, "Second-order sliding-mode control of a Buck converter," in *Proc. IEEE 41st Conf. Decision Control*, 2002, vol. 1, pp. 346–347.
[18] Y. B. Shtessel and R. S. Ashok, "PEM fuel cell/ DC-DC boost power converter system control via traditional and higher order sliding modes," in *Proc. IEEE 50th Eur. Conf. Decision Control*, 2011, pp. 8261–8266.
[19] J. Liu, S. Laghrouche, and M. Wack, "Output high order sliding mode control of unity power factor in three-phase AC/DC boost converter," in *Proc. 12th Int. Workshop Variable Struct. Syst.*, 2012, pp. 76–81.
[20] G. Bartolini, A. Pisano, and E. Usai, "An improved second-order sliding-mode control scheme robust against the measurement noise," *IEEE Trans. Autom. Control*, vol. 49, no. 10, pp. 1731–1737, Oct. 2004.
[21] A. Levant, "Sliding order and sliding accuracy in sliding mode control," *Int. J. Control*, vol. 58, pp. 1247–1263, 1993.
[22] G. Bartolini, A. Pisano, E. Punta, and E. Usai, "A survey of applications of second-order sliding mode control to mechanical systems," *Int. J. Control*, vol. 76, pp. 875–892, 2003.
[23] R. Ling, D. Maksimović, and R. Leyva, "State-machine realization of second-order sliding-mode control for synchronous buck DC-DC converters," *IEEE Energy Conver. Congr. Expo.*, 2013, pp. 125–132.
[24] D. C. Jones and D. Maksimovic, "Second order sliding mode control of a buck converter with output capacitor ESR and ESL," in *Proc. IEEE Workshop Control Model. Power Electron.*, 2014, pp. 1–10.
[25] R. Leyva, D. Maksimović, and R. Ling, "Second-order sliding-mode controller for higher-order DC-DC converters," *IEEE 15th Workshop Control Model. Power Electron.*, 2014, pp. 1–7.
[26] A. Levant, "Higher-order sliding modes, differentiation and output feedback control," *Int. J. Control*, vol. 76, nos. 9/10, pp. 924–941, 2003.
[27] A. Levant, "Principles of 2-sliding mode design," *Automatica*, vol. 43, pp. 576–586, 2007.
[28] A. F. Filippov, *Differential Equations With Discontinuous Right-Hand Side*. Dordrecht, The Netherlands: Kluwer, 1998.

Rui Ling (M'12) received the B.S., M.S., and Ph.D. degrees in automation from Chongqing University, Chongqing, China, in 2002, 2005, and 2009, respectively.

He became a Visiting Scholar at the Colorado Power Electronics Center (CoPEC) in 2012. He is currently an Associate Professor with the Key Laboratory of Dependable Service Computing in Cyber Physical Society (Chongqing University), Ministry of Education and the College of Automation, Chongqing University. He has published more than 20 publications. His current research interests include model and control of renewable energy systems and digital control of switched-mode power converters.

Dragan Maksimovic (M'89–SM'04–F'15) received the B.S. and M.S. degrees in electrical engineering from the University of Belgrade, Belgrade, Serbia (Yugoslavia), in 1984 and 1986, respectively, and the Ph.D. degree from the California Institute of Technology, Pasadena, CA, USA, in 1989.

From 1989 to 1992, he was with the University of Belgrade. Since 1992, he has been with the Department of Electrical, Computer and Energy Engineering, University of Colorado Boulder, Boulder, CO, USA, where he is currently a Professor and Codirector at the Colorado Power Electronics Center (CoPEC). He has coauthored more than 250 publications and the textbook *Fundamentals of Power Electronics* (New York, NY, USA: Springer, 2001). His current research interests include power electronics for renewable energy sources and energy efficiency, high-frequency power conversion using wide bandgap semiconductors, digital control of switched-mode power converters, as well as analog, digital, and mixed-signal integrated circuits for power management applications.

Prof. Maksimovic received the 1997 NSF CAREER Award, the IEEE PELS Transactions Prize Paper Award in 1997, the IEEE PELS Prize Letter Awards in 2009 and 2010, the University of Colorado Inventor of the Year Award in 2006, the IEEE PELS Modeling and Control Technical Achievement Award for 2012, the Holland Excellence in Teaching Awards in 2004 and 2011, the Charles Hutchinson Memorial Teaching Award for 2012, and the 2013 Boulder Faculty Assembly Excellence in Teaching Award.

Ramon Leyva (M'01) received the telecommunication engineering and Ph.D. degrees from Universitat Politècnica de Catalunya, Barcelona, Spain, in 1992 and 2000, respectively.

He became a Visiting Professor with LAAS-CNRS, Toulouse, France (2002–2003, 2009, 2010) and with the COPEC-University of Colorado at Boulder, USA, (2012). He is currently an Associate Professor with the Departament d'Enginyeria en Electrònica, Elèctrica i Automàtica, Universitat Rovira i Virgili, Tarragona, Spain. He has coauthored more than 100 scientific publications, two books and one patent, and has been involved more than 20 R&D projects. His research interests include nonlinear and robust control of power converters and renewable energy.

Dr. Leyva serves as the Reviewer for several IEEE and IET scientific publications.